Preprints.org

Article

Delineating the ultra-low misorientation between the dislocation cellular structures in additively manufactured 316L stainless steel

FEI SUN [*] , Yoshitaka Adachi [*] , Kazuhisa Sato , Takuya Ishimoto , Takayoshi Nakano , Yuichiro Koizumi

Article

Delineating the Ultra-Low Misorientation between the Dislocation Cellular Structures in Additively Manufactured 316L Stainless Steel

Fei Sun [1],*****, **Yoshitaka Adachi** [1],*****, **Kazuhisa Sato** [2], **Takuya Ishimoto** [3], **Takayoshi Nakano** [4,5] and **Yuichiro Koizumi** [4,5]

[1] Department of Material Design Innovation Engineering, Nagoya University, Furo-cho, Chikusa-ku, Nagoya 464-8603, Japan

[2] Research Center for Ultra-High Voltage Electron Microscopy, Osaka University, 7-1 Mihogaoka, Ibaraki, Osaka 567-0047, Japan

[3] Aluminium Research Center, University of Toyama, 3190, Gofuku, Toyama 930-8555, Japan

[4] Division of Materials and Manufacturing Science, Graduate School of Engineering, Osaka University, 2-1 Yamadaoka, Suita, Osaka 565-0871, Japan

[5] Anisotropic Design & Additive Manufacturing Research Center, Osaka University, 2-1 Yamadaoka, Suita, Osaka 565-0871, Japan

***** Correspondence:

Abstract: Sub-micro dislocation cellular structures formed during rapid solidification break the strength-ductility trade-off in laser powder bed fusion (LPBF)-processed 316L stainless steel through high-density dislocations and segregated elements or precipitates at the cellular boundaries. The high-density dislocation entangled at the cellular boundary accommodates solidification strains among the cellular structures and cooling stresses through elastoplastic deformation. Columnar grains with cellular structures typically form along the direction of thermal flux. However, the ultra-low misorientations between the adjacent cellular structures and their interactions with the cellular boundary formation remain unclear. In this study, we revealed the ultra-low misorientations between the cellular structures in LPBF-processed 316L stainless steel using conventional electron backscatter diffraction (EBSD), transmission Kikuchi diffraction (TKD), and transmission electron microscopy (TEM). The conventional EBSD and TKD analysis results could provide the misorientation angles smaller than 2° while the resolution mainly depends on the specimen quality and scanning step size, and so on. TEM technique with higher spatial resolution provides accurate information between adjacent dislocation cells with misorientation angles smaller than 1°. This study presents that TEM method is the better and more precise analysis method of the misorientation measurement of the cellular structures and provides insights into measuring the small misorientation angles between adjacent dislocation cells and nanograins in nanostructured-metals and alloys with ultrafine-grained microstructures.

Keywords: additive manufacturing; cellular structure; misorientation; transmission electron microscopy; transmission Kikuchi diffraction; electron backscatter diffraction

1. Introduction

The intentional manipulation of dislocations through conventional strengthening strategies like grain refinement, solid solution strengthening, and precipitation strengthening plays a pivotal role in tailoring metallic materials for superior performance by effectively introducing extrinsic obstacles to dislocation motion during plastic deformation [1,2]. Dislocation cell is a typical dislocation structure in heavily deformed metallic materials. Its generation and multiplication result from the strain energy reduction of glide dislocations and are associated with the self-organization of discrete dislocations that have become mutually trapped [3]. One of the requirements for dislocation cell formation is that dislocations have sufficient mobility out of their slip plane. During the dislocation cell-forming process, the lattice dislocations re-arrange to minimize the total energy state, forming dense dislocation walls, which act as obstacles to effectively hinder the free movement of dislocations,

leading to increased resistance to deformation [4–7]. The dislocation cells are confined by low-angle grain boundaries [8]. The size of the dislocation cells ranges from several micrometers to the sub-micrometer regime, with size being proportional to the applied stress or strain [9].

Additive manufacturing (AM) processed metallic materials possess various solidification microstructure features spanning a wide range of length scales, involving dislocation cellular structures and a high density of dislocations at an as-built state without plastic deformation. This phenomenon primarily arises from the complex thermal history, enabling large solidification temperature gradients and ultra-high cooling rates during printing. The typical features of dislocation cellular structures involve major high-density cellular boundaries formed by tangled dislocations and minor statistically stored dislocations or dislocation-free in some cases in the cellular interiors. The average dislocation cell size at the cross sections of the dislocation cellular structures ranges from 300nm to 1μm, depending on the laser processing parameters. Many metallic materials processed via AM exhibit ultrafine dislocation cellular structures, leading to extraordinary mechanical properties. In some cases, these materials break the strength-ductility trade-off achieved by the cellular structure with high-density dislocations and solute micro-segregation or precipitate at the cellular boundaries. This achievement represents a significant advancement not easily accessible through traditional processing methods but as a peculiar feature exists widely in additively manufactured metallic materials [10–17]. Note that these dislocation cellular structures are not the same as conventional dislocation cell walls despite the morphology similarities. In addition, during the cellular structure growth process, the dislocations move sufficiently not limited in their slip systems but also out of their slip plane to balance the strain and energy among the surrounding cellular structures, which has been confirmed by the visible tangled dislocations with multiple Burgers vectors under various two-beam observation conditions by transmission electron microscopy (TEM) [17]. The distribution of the cellular structure in the melt pool also mainly contributes to the crystallographic texture of the AM-processed metallic materials [18–20]. However, the misorientations between adjacent cellular structures, the thickness of the cell boundaries, and their interactions with the cellular boundary formation and dislocation density are still open questions to the AM community.

AM technologies for 316L stainless steel (SS) are of great interest due to their high efficiency, design freedom, and better mechanical properties than those manufactured by conventional methods. Laser powder-bed fusion (LPBF) remains the most prevalent technique for metals and alloys compared with other printing methods. The dislocation cellular structure in LPBF-processed 316L SS tends to grow along the maximum temperature gradient from the melt pool boundary (MPB) toward the center of the melt pool and along the preferred growth direction of <001> in the face-centered cubic (FCC) structure. Different laser scanning strategies also make various distribution behaviors of cellular structures, thereby necessitating both imaging and quantitative measurements [10,21–24]. Unlike the traditional large-angle grain boundary, the misorientation across the cellular boundaries in LPBF 316L SS is usually very low [25], and the number of fractions is unavailable to be measured, especially when the ultra-low misorientation is smaller than 2° using conventional electron backscatter diffraction (EBSD). To fully understand the cellular structure behaviors, there remains a question of how to quantitatively measure the misorientations smaller than 2° between the adjacent cellular structures. Traditional techniques like EBSD associated with scanning electron microscopy (SEM) require a large interaction volume between the electrons from the beam and the atoms of the materials, thereby lacking spatial resolution. The transmission Kikuchi diffraction (TKD) technique [26,27] enables the analysis of the microstructure of nanocrystalline materials using an SEM equipped with a standard EBSD system and a special holder for TEM foil installation. The spatial resolution of TKD is higher than conventional EBSD. In addition, transmission electron microscopy (TEM) offers the necessary spatial resolution to observe the nano-sized dislocation cells and obtain the misorientation between the adjacent dislocation cells from Kikuchi-line analysis.

In this study, LPBF-processed 316L SS were carried out to quantitatively evaluate the ultra-low misorientations among the cellular structures using the conventional EBSD, TKD, and TEM

techniques, thereby furthering our understanding of the characteristics of the origin and profuse dislocation cellular structures produced by AM processing in metallic materials.

2. Experimental Procedure

The 316L SS spherical powders were manufactured by gas-atomization with a nominal composition of Fe-18Cr-14Ni-2.5Mo-0.03C (wt.%). The particle sizes were smaller than 53 μm. The 316L SS samples were printed as 10 × 10 × 10 mm cubes by the LPBF fabrication process using a 3D printer (EOSM290, EOS GmbH, Germany) equipped with a Yb-fiber laser. The LPBF processing parameters are shown in Figure 1. Figure 1a displays the schematic diagram of the laser scan strategy, "X-scan strategy", indicating the laser beam was scanned bidirectionally along the X-axis without rotation [28]. Figure 1b lists other LPBF processing parameters of the two samples in terms of laser powder (P), laser scan speed (v), hatch spacing (d) and layer height (t). The volumetric laser energy density (VED) was computed as VED=P/(vdt). The two 316L SS samples have the same VED but have different laser power and hatch spacing. The specimens were cut from the as-printed 316L SS samples to reveal the solidification microstructures of the cross-sections along the build direction (BD), laser scan direction (SD), and transverse direction (TD), then further polished using an automatic polishing machine (PRESI, Mecatech 250 SPI). The polished specimens were electrochemically etched in a solution of nitric and hydrochloric acid (HNO_3:HCl:H_2O= 1:10:10). The characterization of dislocation cellular structure was carried out on the as-built specimens without heat treatment using field emission SEM (FE-SEM, JSM-7001F, JEOL Ltd., Tokyo, Japan) and TEM (JEM-2100PLUS, JEOL Ltd., Tokyo, Japan). TEM specimens were prepared using a focused ion beam (FIB) instrument (Scios2 Dual Beam, Thermo Fisher Scientific, Hillsboro, OR, USA) with Ga ions. Crystallographic orientation of the dislocation cellular structures was analyzed on bulk specimens using EBSD equipped in the FE-SEM. Orientation mapping of the TEM foil was performed using a high-performance focused ion beam system (FIB-SEM, MI-4000L, Hitachi High-Tech. Tokyo, Japan) by TKD technique. The inverse pole figure (IPF) map, kernel average misorientation (KAM) map, and misorientation angle analysis were subsequently analyzed based on the EBSD data using OIM TSL software provided by EDAX. The misorientation angles between adjacent dislocation cells in TEM were evaluated based on the Kikuchi patterns of each dislocation cell, which were collected at the center of each dislocation cell using the tools for orientation determination and crystallographic analysis (TOCA) software package developed by S. Zaefferer [29].

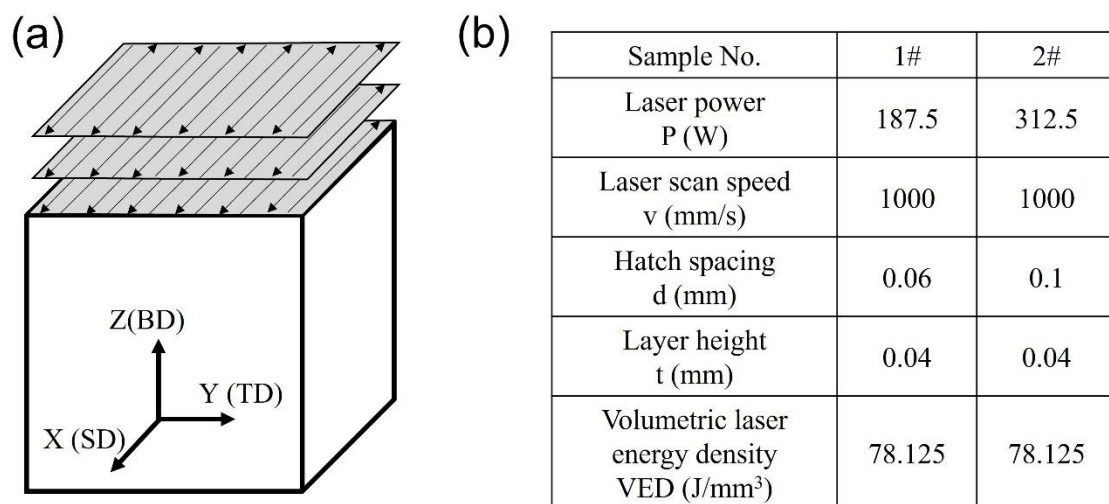| Sample No.	1#	2#
Laser power P (W)	187.5	312.5
Laser scan speed v (mm/s)	1000	1000
Hatch spacing d (mm)	0.06	0.1
Layer height t (mm)	0.04	0.04
Volumetric laser energy density VED (J/mm³)	78.125	78.125

Figure 1. (**a**) Schematic diagram of "X" scan strategy of the LPBF process, (**b**) LPBF parameters of the two samples.

3. Results and Discussion

Figure 2a,b show the SEM images of the solidification microstructure in the YZ cross-section of sample 1 and sample 2, respectively, involving melt pool boundaries and columnar structures. Cellular structures are formed through epitaxial growth along the preferred crystallographic orientation close to the temperature gradient direction from the molt pool boundaries. The dislocation cellular structure has been proven to grow along <100> crystallographic direction in alloys with FCC crystals [30]. Local heat flow enables the complex thermal history and various thermal gradient directions. The cellular structures show different morphologies depending on the direction of observation due to the epitaxial growth. Typical dislocation cells appear when the cellular structure growth direction parallels the observation direction. When the cellular structure growth direction is vertical to the observation direction, the longitudinal section of the cellular structure with a lath-like type is observed. When viewed from other arbitrary planes, the actual sizes of the various dislocation cellular patterns can be deduced from the projection geometry.
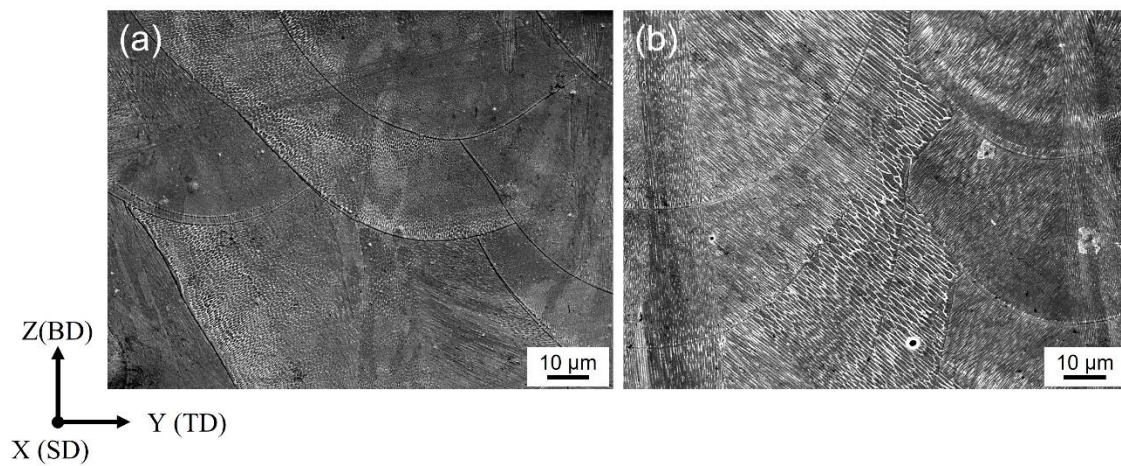

Figure 2. SEM images of the solidification microstructure in (**a**) sample 1 and (**b**) sample 2.

Figure 3 shows the crystallographic texture and orientation according to the EBSD data of the sample 1 fabricated under P=187.5W, v=1000mm/s, d=0.06mm, t=0.04mm, and scan strategy X. Figure 3a shows the IPF map of the YZ cross-section projected in the X direction, acquired with a 1 μm step size. The laser beam size of 100 μm was used in this study, and the hatch spacing in sample 1 is 0.04mm. The latter laser track re-melted most of the previous track and solidified again, causing complex microstructure and crystallographic orientations. Figure 3b shows the related KAM map, measured in degrees, to illustrate a local misorientation and provides a quantitative analysis of the average misorientation angles. It is evident that most structures have local misorientations on the order of 0-1°. Figure 3c shows the corresponding {100}, {110}, and {111} pole figures. The texture tilts in the YZ cross-section by approximately 25° counterclockwise from the building direction toward the subsequent scan track direction. The IPF maps in Figure 3d show that the preferred orientation of FCC structures along the laser scanning direction (X direction) was the [100] direction with the maximum degree of orientation 9.907, indicating the anisotropy feature in this alloy. Figure 3e shows the number fractions of the misorientation angles. The grain boundaries with misorientation angles of 2°–15° are defined as low-angle grain boundaries while the grain boundaries with misorientation angles large than 15° are described as high-angle grain boundaries. The grain boundaries with misorientation of smaller than 2° were not taken into consideration because of the data noise. However, columnar structures with smaller than 1° misorientation in the melt pool were shown in Figure 3f, measured from the local region as indicated by the black arrow in Figure 3a. The misorientation of smaller than 1° was consistent with the KAM map.
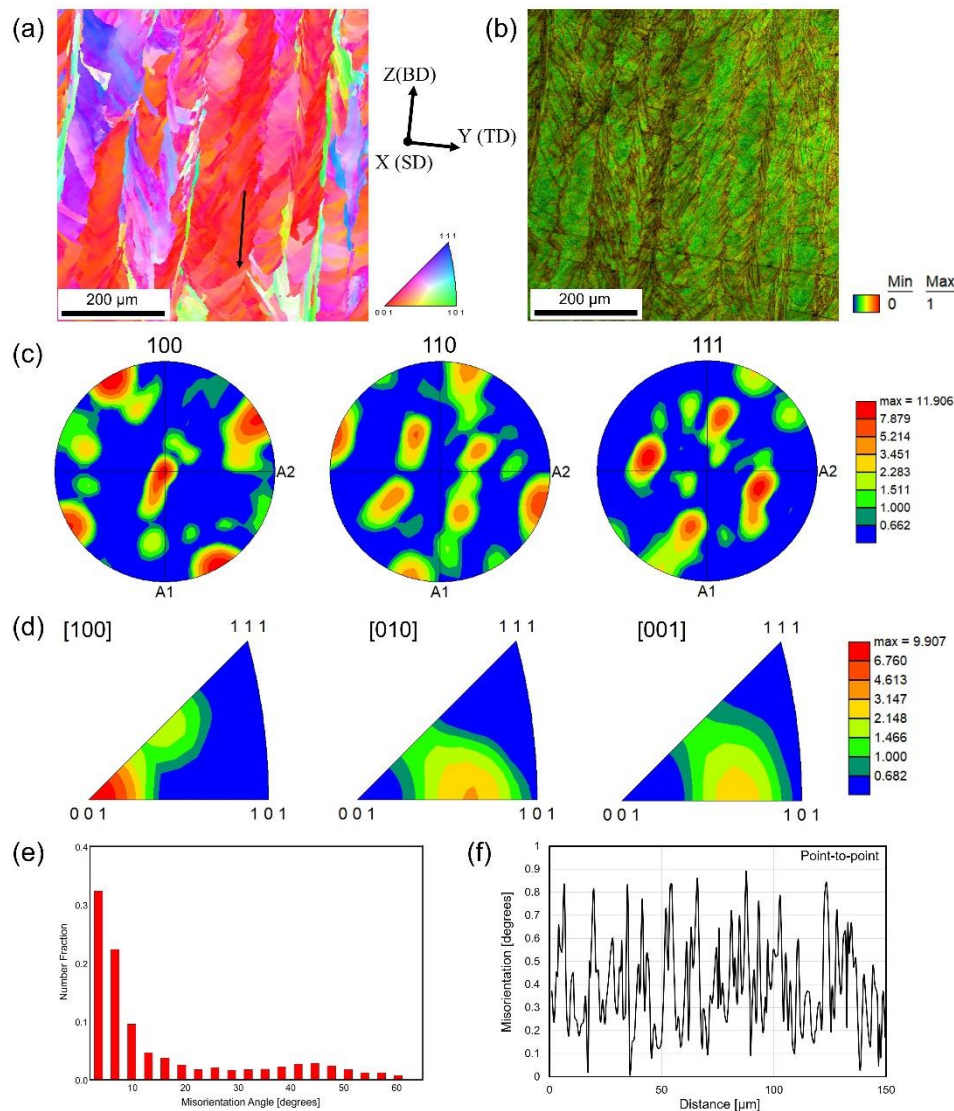
5

Figure 3. EBSD measured results of sample 1: (**a**) Inverse pole figure (IPF) map plotted along the laser scan direction (SD); (**b**) Kernel Average Misorientation (KAM) map measured in degrees from 0° to 1°; (**c**) Pole figures (PF) of crystallographic orientations taken from the YZ plane; (**d**) IPF texture taken from the YZ plane; (**e**) histogram of misorientation angle distribution; (**f**) the point-to-point misorientation along the black arrow shown in (**a**).

Figure 4 shows the crystallographic texture and orientation of the sample 2 fabricated under P=312.5W, v=1000mm/s, d=0.1mm, t=0.04mm, and scan strategy X. Figure 4a shows the IPF map of the YZ cross-section projected in the X direction, acquired with a 1 μm step size. The hatch spacing in sample 2 is 0.1mm, equal to the laser beam size. The latter laser track did not re-melt too much of the previous track and solidified again. Figure 4b shows the related KAM map, measured in degrees, illustrating the local misorientations on the 0°-1° order. Figure 4c shows the corresponding {100}, {110}, and {111} pole figures. The texture tilts in the YZ cross-section by approximately 25° counterclockwise from the building direction toward the subsequent scan track direction. The texture of sample 2 (max MUD = 12.606) was slightly stronger than that of the sample 1 (max MUD = 11.906). The MUD number is one measure of the texture strength in an EBSD pole figure, with higher values indicating stronger alignment. The IPF maps in Figure 4d show that the preferred orientation of FCC structures along the laser scanning direction (X direction) was the [100] direction with a maximum degree of orientation of 10.357, which is higher than that of sample 1. In addition, the building direction (Z direction) displayed the preferred orientation along the [001] direction, which is stronger than sample 1. Figure 4e shows the number fractions of the misorientation angle. The grain

boundaries with misorientation of smaller than 2° were not taken into consideration. However, columnar structures with smaller than 1° misorientation in the melt pool were shown in Figure 4f, measured from the local region as indicated by the black arrow in Figure 4a. The misorientation of smaller than 1° remained consistent with the KAM map.
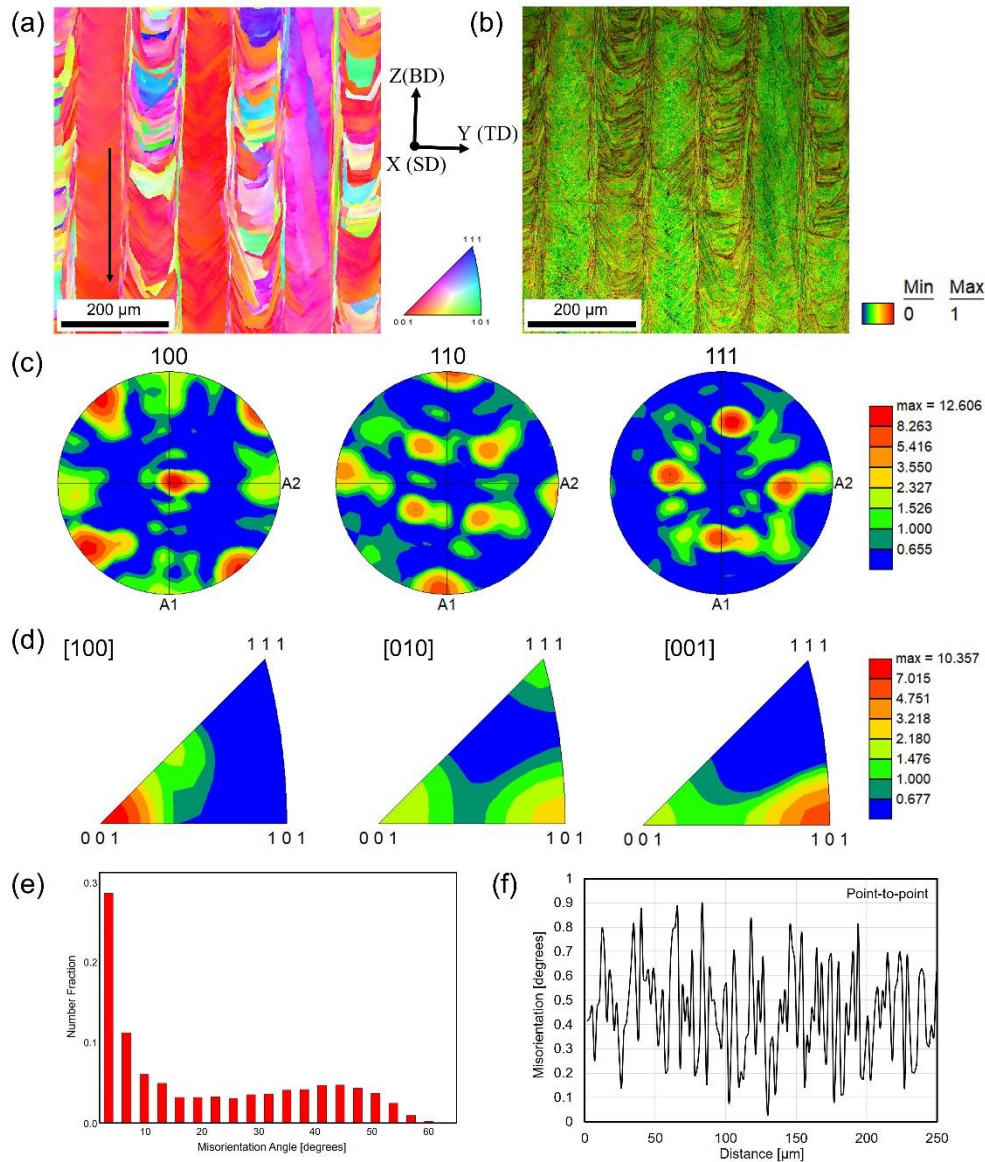

Figure 4. EBSD measured results of sample 2: (**a**) Inverse pole figure (IPF) map plotted along the laser scan direction (SD); (**b**) Kernel Average Misorientation (KAM) map measured in degrees from 0° to 1°; (**c**) Pole figures (PF) of crystallographic orientations taken from the YZ plane; (**d**) IPF texture taken from the YZ plane; (**e**) histogram of misorientation angle distribution; (**f**) the point-to-point misorientation along the black arrow shown in (**a**).

It should be noted that the cellular structures found in the SEM images can be observed but not clearly in the IPF and KAM maps according to the conventional EBSD data. The cellular structures have misorientations smaller than 2°, which usually cannot be detected and measured well. To further explore and take exact analysis of the misorientation of smaller than 2° in the adjacent dislocation cells, we used a TKD technique, also known as transmission EBSD (t-EBSD), to obtain the orientation/misorientation information at high spatial resolution in the TEM samples using a step size of 30 nm. The TEM specimen of the cross-section of the cellular structures of sample 1 for TKD measurement was shown in Figure 5a. In the whole specimen, the thickness decreases from left side to the right side due to the FIB fabrication. Dislocation cells were found clearly in the relative thick

region, while invisible in the very thin region. However, the very thin region is suitable for TKD measurement, so the region indicated by the white square were selected for TKD measurement. Figure 5b shows the IPF map acquired from the t-EBSD data. The grain boundary at right side was demonstrated, while the dislocation cells cannot be detected clearly. Figure 5c shows the related image quality (IQ) map. The dislocation cells remained invisible. Figure 5d,e show the KAM maps with the degree range from 0°-1° and 0°-2°, respectively. A large number fraction of the misorientation smaller than 1° can be identified, even though the dislocation cell boundaries were not detected.
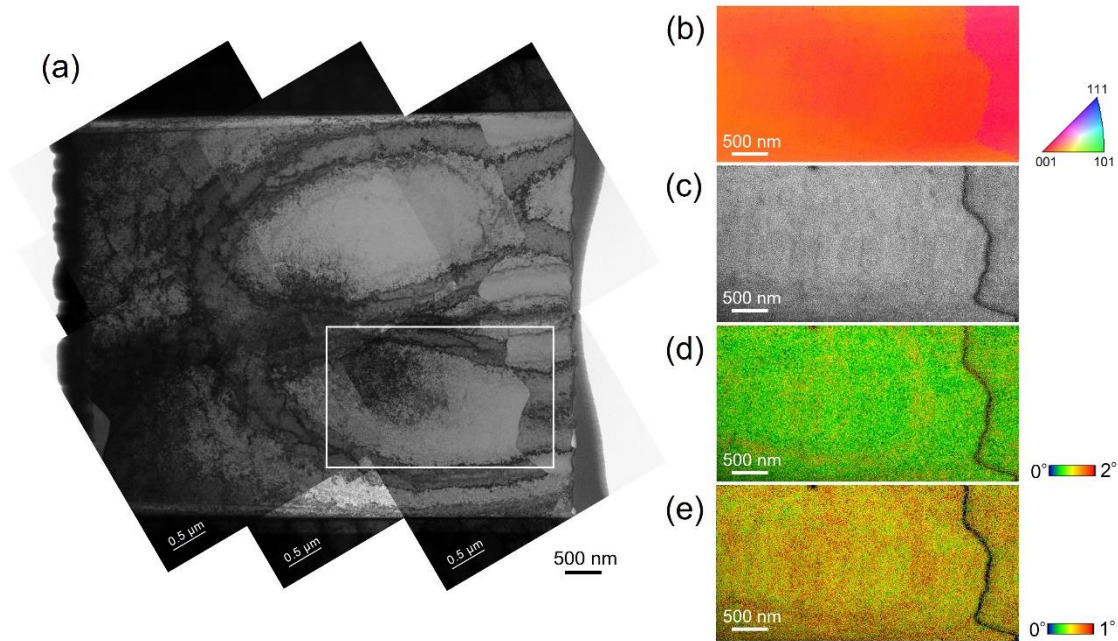

Figure 5. (**a**) TEM bright field image of the dislocation cells along the cross-section of the cellular structure in sample 1; (**b–e**) TKD measurement results of the white square region shown in (**a**), including IPF map, IQ map, KAM map with degree range from 0° to 2°, and 0° to 1°, respectively.

Figure 6a shows the TEM bright field image of the specimen of sample 2 for the TKD measurement. Similarly, the region indicated by the white square was selected for TKD measurement. In this case, the red arrow indicates the cell boundary, which is expected to be detected during the TKD analysis. Figure 6b shows the IPF map, displaying no obvious misorientation. In the IQ map, shown in Figure 6c, the red arrow indicates the cell boundary, which is the same as in Figure 6a. Some slight traces on the left side of the IQ map may display the cell boundaries. Figure 5d,e show the KAM maps with the degree range from 0°-1° and 0°-2°, respectively. Still, a large fraction of the misorientation smaller than 1° can be identified. In Figure 5e, the red arrow indicates the clear misorientation of the cell boundary of the one shown in Figure 5a. Here, the trade-off between in-plane resolution and slice thickness could potentially affect the delineation of the cell structures. The affecting factors may also consist of the surface quality of the TEM specimen, scanning step size, and so on.
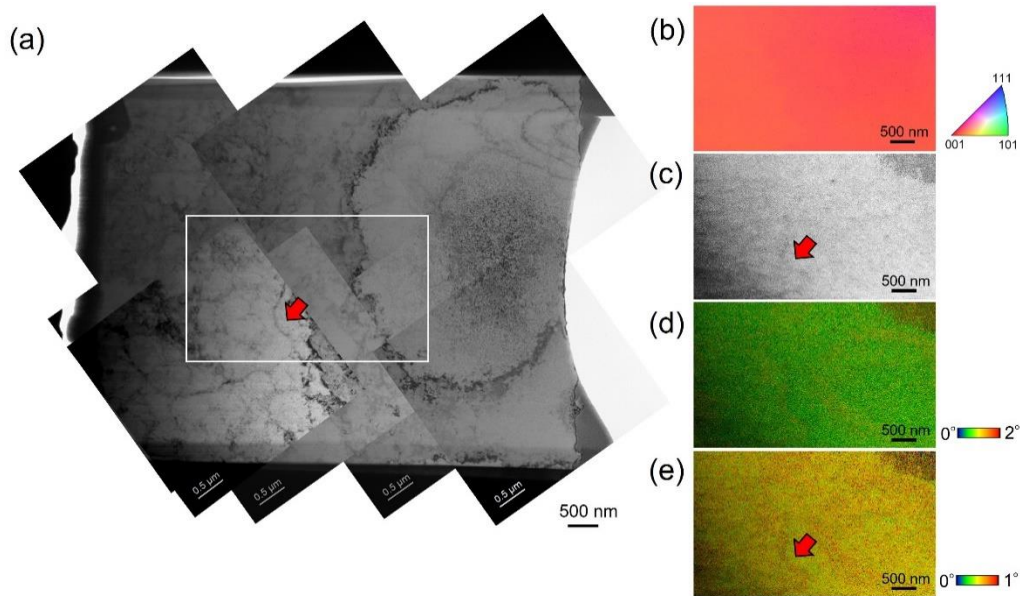
Figure 6. (**a**) TEM bright field image of the dislocation cells along the cross-section of the cellular structure in sample 2; (**b–e**) TKD measurement results of the white square region shown in (**a**), including IPF map, IQ map, KAM map with degree range from 0° to 2°, and 0° to 1°, respectively. Red arrows in (**a,c,e**) indicate the same cell boundary.

To continue analyzing the misorientation between the adjacent dislocation cells, the same TEM specimens of TKD measurement were performed to get the Kikuchi pattern from each dislocation cell for further calculation. Figure 7a shows the TEM bright field image of the dislocation cells from the upper-left region in Figure 5a. The inset diffraction pattern from the whole specimen indicates the single crystal-like structure along [001] direction. The dislocation cells with an average size of 400nm can be observed. Figure 7b shows the schematic diagram of the dislocation cells with numbers from 1 to 20. After getting the Kikuchi pattern, the misorientation between two adjacent dislocation cells was calculated using TOCA software. Figure 7c lists all the misorientations between each dislocation cell. Figure 7d shows the misorientation angle and related number fractions of these dislocation cells. All 20 dislocation cells analyzed have misorientation angles smaller than 0.5°. The misorientation angles ranging from 0.1°-0.2° account for the largest proportion.
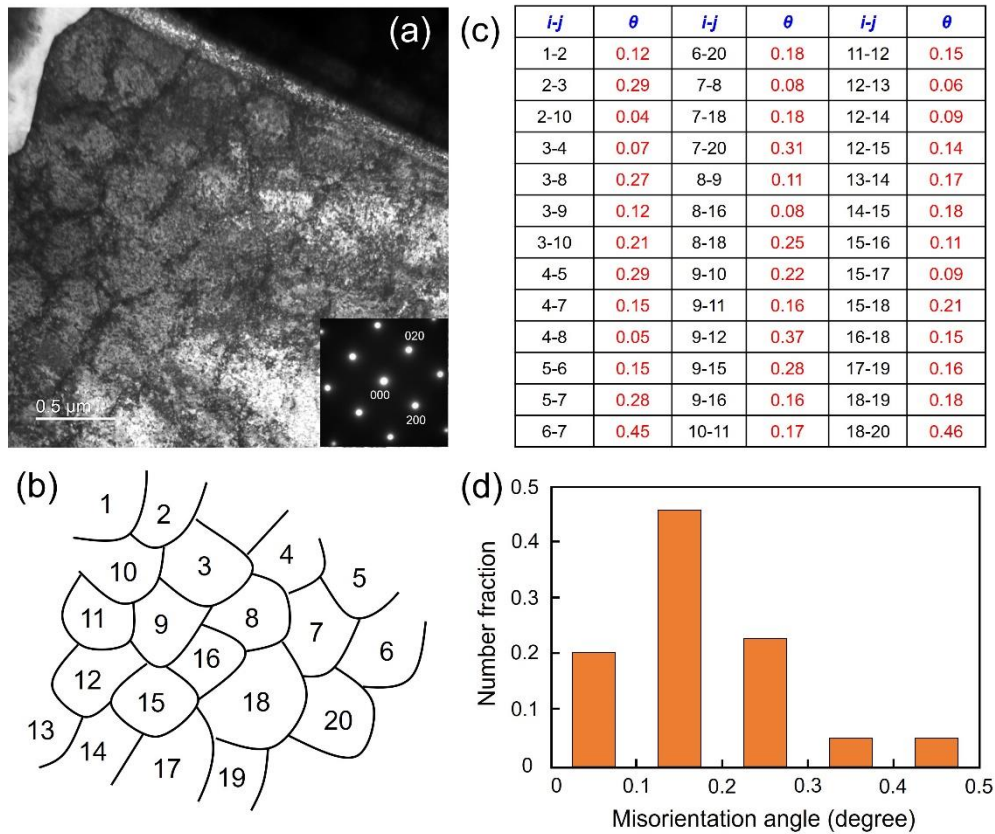
i-j	θ	i-j	θ	i-j	θ
1-2	0.12	6-20	0.18	11-12	0.15
2-3	0.29	7-8	0.08	12-13	0.06
2-10	0.04	7-18	0.18	12-14	0.09
3-4	0.07	7-20	0.31	12-15	0.14
3-8	0.27	8-9	0.11	13-14	0.17
3-9	0.12	8-16	0.08	14-15	0.18
3-10	0.21	8-18	0.25	15-16	0.11
4-5	0.29	9-10	0.22	15-17	0.09
4-7	0.15	9-11	0.16	15-18	0.21
4-8	0.05	9-12	0.37	16-18	0.15
5-6	0.15	9-15	0.28	17-19	0.16
5-7	0.28	9-16	0.16	18-19	0.18
6-7	0.45	10-11	0.17	18-20	0.46

Figure 7. (**a**) TEM bright field of dislocation cells and related diffraction pattern of sample 1; (**b**) schematic diagram of the dislocation cells with indexing from 1 to 20; (**c**) calculated misorientation angle θ between adjacent cells *i* and *j*; (**d**) histogram of misorientation angle distribution.

Figure 8a shows the TEM bright field image of the dislocation cells from the lower-left region in Figure 6a. The inset diffraction pattern from the whole specimen indicates the single crystal-like structure along [001] direction. The dislocation cells with an average size of 400nm can also be observed. Figure 8b shows the schematic diagram of the dislocation cells with numbers from 1 to 30. Figure 8c lists all the misorientations between each dislocation cell. Figure 8d shows the misorientation angle and related number fractions of these dislocation cells. All 20 analyzed dislocation cells have misorientation angles ranging from 0° to 0.9°. The misorientation angles range from 0.1°-0.2° also account for the largest proportion.
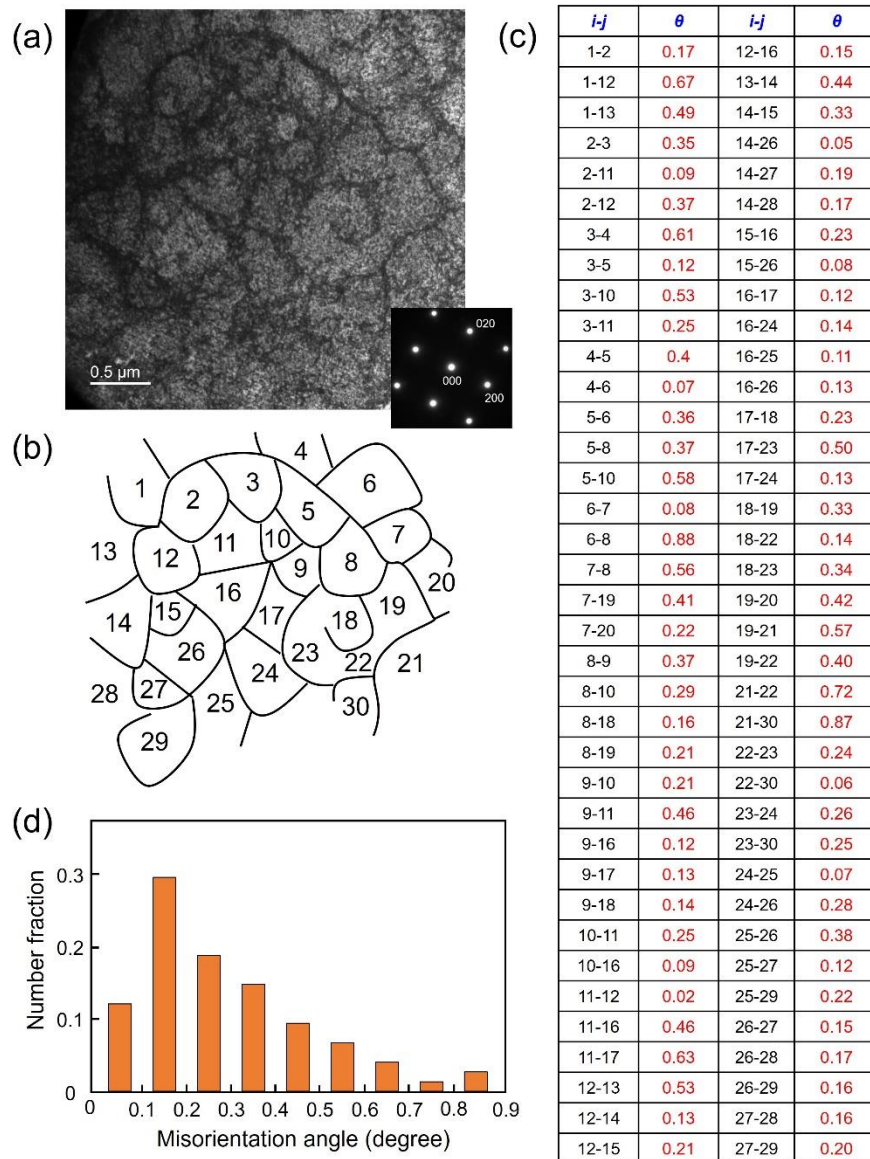
(a)

(c)

i-j	θ	i-j	θ
1-2	0.17	12-16	0.15
1-12	0.67	13-14	0.44
1-13	0.49	14-15	0.33
2-3	0.35	14-26	0.05
2-11	0.09	14-27	0.19
2-12	0.37	14-28	0.17
3-4	0.61	15-16	0.23
3-5	0.12	15-26	0.08
3-10	0.53	16-17	0.12
3-11	0.25	16-24	0.14
4-5	0.4	16-25	0.11
4-6	0.07	16-26	0.13
5-6	0.36	17-18	0.23
5-8	0.37	17-23	0.50
5-10	0.58	17-24	0.13
6-7	0.08	18-19	0.33
6-8	0.88	18-22	0.14
7-8	0.56	18-23	0.34
7-19	0.41	19-20	0.42
7-20	0.22	19-21	0.57
8-9	0.37	19-22	0.40
8-10	0.29	21-22	0.72
8-18	0.16	21-30	0.87
8-19	0.21	22-23	0.24
9-10	0.21	22-30	0.06
9-11	0.46	23-24	0.26
9-16	0.12	23-30	0.25
9-17	0.13	24-25	0.07
9-18	0.14	24-26	0.28
10-11	0.25	25-26	0.38
10-16	0.09	25-27	0.12
11-12	0.02	25-29	0.22
11-16	0.46	26-27	0.15
11-17	0.63	26-28	0.17
12-13	0.53	26-29	0.16
12-14	0.13	27-28	0.16
12-15	0.21	27-29	0.20

(b)

(d)

Figure 8. (**a**) TEM bright field of dislocation cells and related diffraction pattern of sample 2; (**b**) schematic diagram of the dislocation cells with indexing from 1 to 30; (**c**) calculated misorientation angles θ between adjacent cells *i* and *j*; (**d**) histogram of misorientation angle distribution.

4. Conclusions

This study analyzed the misorientation angles between cellular structure in LPBF processed 316L SS, mainly ranging from 0°-2° by conventional EBSD, TKD and TEM techniques. The conventional EBSD technique presents the misorientations in IPF map between the cellular structures without consideration of the angle smaller than 2°. KAM map and misorientation analysis of point to point could display the misorientations smaller than 1°. TKD analysis results with higher in-plane resolution still cannot display the misorientations between the adjacent dislocation cells and also present misorientations smaller than 1°. It's affecting factors may include surface quality and thickness of the TEM specimen, scanning step size, and so on. TEM analysis results show the accurate misorientation angles between adjacent dislocation cells according to the Kikuchi pattern acquired from each dislocation cell. The misorientation angles have been identified with the range from 0°-0.5° in sample 1 and 0°-0.9° in sample 2. The misorientation angles range from 0.1°-0.2° also account for the largest proportion in both samples. This study presents that TEM method is the better and more accurate analysis method of the measurement of the cellular structures and provides insights into

measuring the small misorientation angle between adjacent dislocation cells and nanograins in nanostructured metals and alloys with ultrafine-grained microstructures.

References

1. Argon, A. *Strengthening Mechanisms in Crystal Plasticity*, Oxford University Press: Oxford, 2012.
2. Meyers, M.A.; Chawla, K.K. *Mechanical Behavior of Materials*, Cambridge University Press: Cambridge, 2008.
3. Kuhlmann-Wilsdorf, D., Van der Merwe, J. H. Theory of dislocation cell sizes in deformed metals. *Mater. Sci. Eng.* **1982**, *55*, 79–83.
4. Kuhlmann-Wilsdorf, D. Work hardening; Gordon and Breach: New York, USA, 1968; pp. 97.
5. Hirsch, P. B. Internal Stresses and Fatigue in Metals; Elsevier: New York, USA, 1958; pp. 138.
6. Swann, P. R. Electron Microscopy and Strength of Crystals; Interscience: New York, USA, 1963; pp. 131.
7. Holt, D. L. Dislocation cell formation in metals. *J.Appl.Phys.* **1970**, *41*, 3197-3201.
8. Tao, N.R.; Wang, Z.B.; Tong, W.P.; Sui, M.L.; Lu, J.; Lu, K. An investigation of surface nanocrystallization mechanism in Fe induced by surface mechanical attrition treatment. *Acta Mater.* **2002**, *50*, 4603–4616.
9. Kuhlmann-Wilsdorf, D. Theory of plastic deformation: -properties of low energy dislocation structures. *Mater. Sci. Eng. A.* **1989**, *113*, 1–41.
10. Wang, Y.M.; Voisin, T.; McKeown, J.T.; Ye, J.; Calta, N.P.; Li, Z.; Zeng, Z.; Zhang, Y.; Chen, W.; Roehling, T.T.; Ott, R.T.; Santala, M. K.; Depond, P.J.; Matthews, M.J.; Hamza, A.V.; Zhu, T. Additively manufactured hierarchical stainless steels with high strength and ductility. *Nature Mater.* **2018**, *17*, 63–71.
11. Liu, L.; Ding, Q.; Zhong, Y.; Zou, J.; Wu, J.; Chiu, Y.L.; Li, J.; Zhang, Z.; Yu, Q. Shen, Z. Dislocation network in additive manufactured steel breaks strength–ductility trade-off. *Mater. Today* **2018** *21*, 354–361.
12. Zhu, Z.G.; Nguyen, Q.B.; Ng, F.L.; An, X.H.; Liao, X.Z.; Liaw, P.K.; Nai, S.M.L.; Wei J. Hierarchical microstructure and strengthening mechanisms of a CoCrFeNiMn high entropy alloy additively manufactured by selective laser melting. *Scr. Mater.* **2018**, *154*, 20–24.
13. Wang, H.; Zhu, Z.G.; Chen, H.; Wang, A.G.; Liu, J.Q.; Liu, H.W.; Zheng, R.K.; Nai, S.M.L.; Primig, S.; Babu, S.S.; Ringer, S.P.; Liao X.Z. Effect of cyclic rapid thermal loadings on the microstructural evolution of a CrMnFeCoNi high-entropy alloy manufactured by selective laser melting. *Acta Mater.* **2020**, *196*, 609–625.
14. Gallmeyer, T.G.; Moorthy, S.; Kappes, B. B.; Mills, M. J.; Amin-Ahmadi, B.; Stebner A.P. Knowledge of process-structure-property relationships to engineer better heat treatments for laser powder bed fusion additive manufactured Inconel 718. *Addit. Manuf.* **2020**, *31*, 100977.
15. Bertsch, K.M.; Meric de Bellefon, G.; Kuehl, B.; Thoma D.J. Origin of dislocation structures in an additively manufactured austenitic stainless steel 316L. *Acta Mater.* **2020**, *199*,19–33.
16. Sun, Z.; Tan, X.; Tor, S.B.; Chua, C.K. Simultaneously enhanced strength and ductility for 3D-printed stainless steel 316L by selective laser melting. *NPG Asia Mater.* **2018**, *10*, 127–136.
17. Sun, F.; Ogawa, T.; Adachi, Y.; Sato, K.; Takagi, S.; Miyamoto, G.; Suzuki, A.; Yamanaka, A.; Nakada, N.; Ishimoto, T.; Nakano, T.; Koizumi, Y. Modulated structure formation in dislocation cells in 316L stainless steel fabricated by laser powder bed fusion. *Mater. Trans.* **2023**, *64*, 1143–1149.
18. Hagihara, K.; Takayoshi Nakano, T. Control of Anisotropic Crystallographic Texture in Powder Bed Fusion Additive Manufacturing of Metals and Ceramics--A Review. *JOM*, **2022**, *74*, 1760–1773.
19. Gokcekaya, O.; Ishimoto, T.; Hibino, S.; Yasutomi, J.; Narushima, T.; Nakano, T. Unique crystallographic texture formation in Inconel 718 by laser powder bed fusion and its effect on mechanical anisotropy. *Acta Mater.* **2021**, *212*, 116876.
20. Sun, S.; Ishimoto, T.; Hagihara, K.; Tsutsumi, Y.; Hanawa, T.; Nakano, T. Excellent mechanical and corrosion properties of austenitic stainless steel with a unique crystallographic lamellar microstructure via selective laser melting. *Scripta Mater.* **2019**, *159*, 89–93.
21. Shamsujjoha, M.; Agnew, S.R.; Fitz-Gerald, J.M.; Moore, W.R.; Newman, T.A. High strength and ductility of additively manufactured 316l stainless steel explained. *Metall. Mater. Trans. A* **2018**, *49*, 3011–3027.
22. Wang, F.; Stinville, J-C.; Charpagne, M-agathe; Echlin, M.; Agnew, S.; Pollock, T.; Graef, M.; Gianola, D. Dislocation cells in additively manufactured metallic alloys characterized by electron backscatter diffraction pattern sharpness. *Mater. Charact.* **2023**, *197*, 112673.

23. Kim, R.E.; Moon, J.; Kim, E.S.; Lee, J.; Kim, H.S. Surface heterostructuring of laser-clad 316L stainless steel through texture-driven deformation twinning. *Scripta Mater.* **2022**, *221*, 114989.

24. Marattukalam, J.J.; Karlsson, D.; Pacheco, V.; Beran, P.; Wiklund, U.; Jansson, U.; Hjörvarsson, B.; Sahlberg, M. The effect of laser scanning strategies on texture, mechanical properties, and site-specific grain orientation in selective laser melted 316L SS. *Mater. Des.* **2020**, *193*, 108852.

25. Kong, D.; Dong, C.; Ni, X.; Liang, Z.; Man, C.; Li, X. Bio-functional and anti-corrosive 3D printing 316L stainless steel fabricated by selective laser melting. *Mater. Res. Lett.* **2020**, *8*, 390–397.

26. Keller, R.R.; Geiss, R.H. Transmission EBSD from 10 nm domains in a scanning electron microscope. *J. Microsc.* **2012**, *245*, 245–251.

27. Sun, F. Integrated TEM/transmission-EBS for recrystallization analysis in nickel-based disc superalloy. *Prog. Nat. Sci.: Mater.* **2021**, *31*, 63–67.

28. Ishimoto, T.; Wu, S.Q.; Ito, Y.; Sun, S.H.; Amano, H.; Nakano, T. Crystallographic orientation control of 316L austenitic stainless steel via selective laser melting. *ISIJ Inter.* **2020**, *60*, 1758–1764.

29. Zaefferer, S. New developments of computer-aided crystallographic analysis in transmission electron microscopy. *J. Appl. Cryst.* **2000**, *33*, 10–25.

30. Sprouster, D. J., Cunningham, W. S., Halada, G. P., Yan, H., Pattammattel, A., Huang, X., Olds, D; Tilton, M.; Chu, Y. S.; Dooryhee, E.; Manogharan, G. P.; Trelewicz, J. R. Dislocation microstructure and its influence on corrosion behavior in laser additively manufactured 316L stainless steel. *Addit. Manuf.* **2021**, *47*, 102263.